CrossMark

THE DISCOVERY OF LENSED RADIO AND X-RAY SOURCES BEHIND THE FRONTIER FIELDS CLUSTER MACS J0717.5+3745 WITH THE JVLA AND *CHANDRA*

R. J. VAN WEEREN[1,17], G. A. OGREAN[1,18], C. JONES[1], W. R. FORMAN[1], F. ANDRADE-SANTOS[1], A. BONAFEDE[2], M. BRÜGGEN[2], E. BULBUL[1], T. E. CLARKE[3], E. CHURAZOV[4,5], L. DAVID[1], W. A. DAWSON[6], M. DONAHUE[7], A. GOULDING[8], R. P. KRAFT[1], B. MASON[9], J. MERTEN[10], T. MROCZKOWSKI[3,19], S. S. MURRAY[1,11], P. E. J. NULSEN[1,12], P. ROSATI[13], E. ROEDIGER[14,20], S. W. RANDALL[1], J. SAYERS[15], K. UMETSU[16], A. VIKHLININ[1], AND A. ZITRIN[15,18]

[1] Harvard-Smithsonian Center for Astrophysics, 60 Garden Street, Cambridge, MA 02138, USA; rvanweeren@cfa.harvard.edu
[2] Hamburger Sternwarte, Universität Hamburg, Gojenbergsweg 112, D-21029 Hamburg, Germany
[3] U.S. Naval Research Laboratory, 4555 Overlook Ave SW, Washington, DC 20375, USA
[4] Max Planck Institute for Astrophysics, Karl-Schwarzschild-Str. 1, D-85741, Garching, Germany
[5] Space Research Institute, Profsoyuznaya 84/32, Moscow, 117997, Russia
[6] Lawrence Livermore National Lab, 7000 East Avenue, Livermore, CA 94550, USA
[7] Department of Physics and Astronomy, Michigan State University, East Lansing, MI 48824, USA
[8] Department of Astrophysical Sciences, Princeton University, Princeton, NJ 08544, USA
[9] National Radio Astronomy Observatory, 520 Edgemont Road, Charlottesville, VA 22903, USA
[10] Department of Physics, University of Oxford, Keble Road, Oxford OX1 3RH, UK
[11] Department of Physics and Astronomy, Johns Hopkins University, 3400 North Charles Street, Baltimore, MD 21218, USA
[12] ICRAR, University of Western Australia, 35 Stirling Hwy, Crawley WA 6009, Australia
[13] Dipartimento di Fisica e Scienze della Terra, Università di Ferrara, Via Saragat 1, I-44122 Ferrara, Italy
[14] E.A. Milne Centre for Astrophysics, Department of Physics & Mathematics, University of Hull, Cottinton Road, Hull, HU6 7RX, UK
[15] Cahill Center for Astronomy and Astrophysics, California Institute of Technology, MC 249-17, Pasadena, CA 91125, USA
[16] Institute of Astronomy and Astrophysics, Academia Sinica, P.O. Box 23-141, Taipei 10617, Taiwan

ABSTRACT

We report on high-resolution *JVLA* and *Chandra* observations of the *Hubble Space Telescope* (*HST*) Frontier Cluster MACS J0717.5+3745. MACS J0717.5+3745 offers the largest contiguous magnified area of any known cluster, making it a promising target to search for lensed radio and X-ray sources. With the high-resolution 1.0–6.5 GHz *JVLA* imaging in A and B configuration, we detect a total of 51 compact radio sources within the area covered by the *HST* imaging. Within this sample, we find seven lensed sources with amplification factors larger than two. None of these sources are identified as multiply lensed. Based on the radio luminosities, the majority of these sources are likely star-forming galaxies with star-formation rates (SFRs) of 10–50 $M_\odot$ yr^{-1} located at $1 \lesssim z \lesssim 2$. Two of the lensed radio sources are also detected in the *Chandra* image of the cluster. These two sources are likely active galactic nuclei, given their 2–10 keV X-ray luminosities of $\sim 10^{43-44}$ erg s^{-1}. From the derived radio luminosity function, we find evidence for an increase in the number density of radio sources at $0.6 < z < 2.0$, compared to a $z < 0.3$ sample. Our observations indicate that deep radio imaging of lensing clusters can be used to study star-forming galaxies, with SFRs as low as $\sim 10\ M_\odot$ yr^{-1}, at the peak of cosmic star formation history.

Key words: galaxies: clusters: individual (MACS J0717.5+3745) – gravitational lensing: strong – radio continuum: galaxies

1. INTRODUCTION

Strong lensing clusters are excellent targets to study high-redshift galaxies due to their large magnification. This offers the advantage of studying these sources at improved spatial resolution and allows the detection of very faint sources due to the amplification of their integrated fluxes (for a review, see Kneib & Natarajan 2011).

Most blind searches for lensed galaxies behind galaxy clusters have traditionally been carried out at optical, near-infrared (near-IR), and submillimeter wavelengths, with the submillimeter observations mostly targeting rare but very luminous dusty galaxies with high star-formation rates (SFRs). Very few blind and deep studies have been carried out at radio or X-ray wavelengths. One likely reason for this is that the number of lensed active galactic nuclei (AGNs) is much lower than that of typical lensed galaxies that are observed at optical and near-IR wavelengths.

Non-thermal radio emission is also emitted by the more numerous star-forming galaxies, with the radio luminosity correlating with the SFR (e.g., Condon 1992; Bell 2003; Garn et al. 2009). Such studies have the advantage of being free from dust extinction. The cosmic SFR increases with redshift, peaking at $z \sim 2$ (for a recent review, see Madau & Dickinson 2014). However, at $z \sim 2$, only the "tip of the iceberg" can be currently observed, with extreme SFR of $\gtrsim 10^2$ $M_\odot$ yr^{-1}. A more typical star-forming galaxy, with SFR $\sim 10\ M_\odot$ yr^{-1} at $z \sim 1.5$, has an integrated flux density of about one μJy at 3 GHz, below the detection limit of the current generation radio telescopes. However, with the power of lensing, these galaxies should come within reach of deep Jansky Very Large Array (*JVLA*) observations. Combining deep *JVLA* imaging with lensing will therefore be the only way to study these more typical SF galaxies in the radio at the peak of cosmic SF before the advent of the Square Kilometre Array.

---

[17] Einstein Fellow.
[18] Hubble Fellow.
[19] National Research Council Fellow.
[20] Visiting Scientist.

Table 1
JVLA Observations

	L-band A-array	S-band A-array	S-band B-array	C-band B-array
Observation dates	2013 Mar 28	2013 Feb 22	2013 Nov 5	2013 Sep 30
Frequencies coverage (GHz)	1–2	2–4	2–4	4.5–6.5
On source time (hr)	∼5	∼5	∼5	∼5
Correlations	full stokes	full stokes	full stokes	full stokes
Channel width (MHz)	1	2	2	2
Integration time (s)	1	1	3	3
LAS (arcsec)	36	18	58	29

MACS J0717.5+3745 was discovered by Edge et al. (2003) as part of the MAssive Cluster Survey (MACS; Ebeling et al. 2001). It is an extremely massive, hot merging galaxy cluster located at $z = 0.5458$, with a global temperature of 11.6 ± 0.5 keV (Ebeling et al. 2007). A large-scale galaxy filament that is connected to the cluster, with a projected length of ∼4.5 Mpc, has also been reported (Ebeling et al. 2004; Jauzac et al. 2012). The cluster is one of the most complex and dynamically disturbed clusters known, with the merger involving four separate substructures and shock-heated ∼20 keV gas (Ma et al. 2008, 2009; Limousin et al. 2012).

The large total mass of $M_{\mathrm{vir}} = (3.5 \pm 0.6) \times 10^{15} \, M_{\odot}$ (Umetsu et al. 2014) and relatively shallow mass profile of the cluster boosts the gravitational lens magnification and results in a total lensed area that is about 3.5 arcmin^2 for a galaxy located at $z \sim 8$. This area is higher than any other known massive cluster (Zitrin et al. 2009a). For this reason, the cluster is also part of the Cluster Lensing And Supernova survey with Hubble (CLASH; Postman et al. 2012; Medezinski et al. 2013) and the *Hubble Space Telescope* (*HST*) Frontier Fields program.[21]

Since MACS J0717.5+3745 is the largest known cosmic lens, it is a prime target to search for radio and X-ray emission associated with lensed background galaxies. In this work, we present deep high-resolution *JVLA* observations which can be used for this purpose. In addition, we carry out a search for lensed X-ray sources with newly acquired deep *Chandra* data. We adopt a ΛCDM cosmology with $H_0 = 70 \, \mathrm{km \, s^{-1} \, Mpc^{-1}}$, $\Omega_{\mathrm{m}} = 0.3$, and $\Omega_{\Lambda} = 0.7$. With this cosmology, $1''$ corresponds to a physical scale of 6.387 kpc at $z = 0.5458$.

2. OBSERVATIONS AND DATA REDUCTION

2.1. JVLA Observations

JVLA observations of MACS J07175+3745 were obtained in the L-band (1–2 GHz) in the A-array configuration, in the S-band (2–4 GHz) in the A- and B-array configurations, and in the C-band (4.5–6.5 GHz) in the B-array configuration. All observations were done using single 6 hr runs, resulting in a typical on-source time of ∼5 hr. The total recorded bandwidth was 1 GHz for the L-band, and 2 GHz for the S- and C-bands. The primary calibrators were 3C138 and 3C147. The secondary calibrator (J0713+4349) was observed for a couple of minutes at 30–40 minute intervals. All four circular polarization products were recorded. An overview of the observations is given in Table 1.

The data were reduced with CASA version 4.2.1 (McMullin et al. 2007). The data from the different observing runs were all reduced in the same way. For the two primary calibrators, we used the clean-component models provided by CASA. We also took the overall spectral index of the primary calibrator sources into account, scaling the flux density for each channel.

As a first step, the data were Hanning smoothed and pre-determined elevation-dependent gain tables and antenna position offsets were applied. This was followed by automatic flagging of radio frequency interference (RFI) using the *tfcrop* mode of the CASA task flagdata. We then determined an initial bandpass correction using 3C147. This bandpass was applied and additional RFI was identified and flagged with the AOFlagger (Offringa et al. 2010). The reason for applying the bandpass is to avoid flagging good data due to the bandpass roll off at the edges of the spectral windows.

Next, we determined complex gain solutions on 3C147 for the central 10 channels of each spectral window to remove possible time variations of the gains during the calibrator observations. We pre-applied these solutions to find the delay terms (gaintype = "K") and bandpass calibration. Applying the bandpass and delay solutions, we re-determined the complex gain solutions for both primary calibrators using the full bandwidth. We then determined the global cross-hand delay solutions (gaintype = "KCROSS") from the polarized calibrator 3C138. For 3C138, we assumed a rotation measure (RM) of 0 rad m^{-1}, and for the RL-phase difference we took $-15°$. All relevant solutions tables were applied on the fly to determine the complex gain solution for the secondary calibrator J0713+4349 and to establish its flux density scale accordingly. The absolute flux scale uncertainty due to bootstrapping from the calibrators is assumed to be a few percent (Perley & Butler 2013). As a next step, we used J0713+4349 to find the channel-dependent polarization leakage terms. 3C138 was used to perform the polarization angle calibration for each channel.[22] Finally, all solutions were applied to the target field. The corrected data were then averaged by a factor of 3 in time and a factor of 6 in frequency.

To refine the calibration for the target field, we performed three rounds of phase-only self-calibration and a final round of amplitude and phase self-calibration. For the imaging we employed w-projection (Cornwell et al. 2008, 2005) to take the non-coplanar nature of the array into account. Image sizes of up to 12288^2 pixels were needed (A-array configuration) to deconvolve a few bright sources outside the main lobe of the primary beam. For each frequency band, the full bandwidth was used to make a single deep Stokes I continuum image. We used Briggs (1995) weighting with a robust factor of 0. The spectral index was taken into account during the deconvolution of each observing run (nterms = 3; Rau & Cornwell 2011). We manually flagged some additional data during the self-calibration process by visually inspecting the self-calibration

---

[22] The polarization observations will be discussed in a forthcoming paper.

Table 2
Image Properties

	L-band A-array	S-band A+B-array	C-band B-array
Resolution (arcsec × arcsec)	1.5 × 1.3	1.04 × 0.79	1.80 × 1.38
Noise (μJy beam^{-1})	5.2	1.8	1.9

Table 3
Summary of the *Chandra* Observations

ObsID	Instrument	Mode	Start Date	Exposure Time (ks)	Filtered Exposure Time (ks)
1655	ACIS-I	FAINT	2001 Jan 29	19.87	17.06
4200	ACIS-I	VFAINT	2004 Jan 10	59.04	58.02
16235	ACIS-I	FAINT	2013 Dec 16	70.16	68.37
16305	ACIS-I	VFAINT	2013 Dec 11	94.34	90.42

solutions. Clean masks were employed during the deconvolution. The clean masks were made with the PyBDSM source detection package (Mohan & Rafferty 2015). The S-band A-array and B-array configuration data were combined after the self-calibration to make a single deep 2–4 GHz image. The final images were made with Briggs weighting and a robust factor of 0.75, except for the C-band image, for which we employed natural weighting. Images were corrected for the primary beam attenuation, with the frequency dependence of the beam taken into account. An overview of the resulting image properties, such as rms noise and resolution, is given in Table 2.

2.2. Chandra Observations

MACS J0717.5+3745 was observed with *Chandra* for a total of 243 ks between 2001 and 2013. A summary of the observations is presented in Table 3. The data sets were reduced with CIAO v4.7 and CALDB v4.6.5, following the same methodology that was described by Ogrean et al. (2015).

Point sources were detected with the CIAO script *wavdetect* in the energy bands 0.5–2 and 2–7 keV, using wavelet scales of 1, 2, 4, 8, 16, and 32 pixels and ellipses with radii 5σ around the centers of the detected sources. Due to the complicated morphology of MACS J0717.5+3745, all sources found by *wavdetect* were visually inspected and some false detections associated with the extended ICM of the cluster were removed. The local background around each point source was described using an elliptical annulus with an inner radius equal to the source radius and an outer radius approximately ~3 times larger than the source radius. To model the X-ray spectra of the point sources, the local background spectra were subtracted from the corresponding source spectra. The spectra were binned to a minimum of one count/bin, and modeled with XSPEC v12.8.2 using the extended C-statistics[23] (Cash 1979; Wachter et al. 1979). All the source spectra were modeled as power laws and included galactic absorption. The hydrogen column density in the direction of MACS J0717.5+3745 was fixed to 8.4×10^{20} cm^{-2}, which is the sum of the weighted average atomic hydrogen column density from the Leiden–Argentine–Bonn (LAB; Kalberla et al. 2005) Survey and the molecular hydrogen column density determined by Willingale et al. (2013) from *Swift* data.

X-ray fluxes and luminosities were calculated in the energy band 2–10 keV, with uncertainties quoted at the 90% confidence level.

3. RESULTS

The 2–4 GHz S-band image of the cluster region is shown in Figure 1. The most prominent source in the images is a large filamentary radio relic that is associated with the cluster MACS J0717.5+3745. At the center of this relic, a narrow angle tail (NAT) galaxy is visible, which is associated with a cluster member at $z = 0.5528$ (Ebeling et al. 2014). Another tailed radio source ($z = 0.5399$; Ebeling et al. 2014) is visible at the far SE corner of the image. A bright linearly shaped FRI-type radio source (Fanaroff & Riley 1974) is located to the SE. This source is associated with an elliptical foreground galaxy (2MASX J07173724+3744224) located at $z = 0.1546$ (Bonafede et al. 2009). The radio relics and tailed radio galaxies belonging to MACS J0717.5+3745 will be discussed in a separate paper (R. J. van Weeren et al. 2015, in preparation).

3.1. Source Detection

We used the PyBDSM[24] source detection package to find and determine the integrated flux densities of the radio sources in the images. PyBDSM identifies "islands" of contiguous pixels above a detection threshold and fits each island with Gaussians.

For detecting these islands, we took a threshold of $3\sigma_{rms}$ and a pixel threshold of $4\sigma_{rms}$, meaning that at least one pixel in each island needs to exceed the local background by $4\sigma_{rms}$. We determined the local rms noise using a sliding box with a size of 300 pixels to take the noise increase by the primary beam attenuation into account. We manually inspected the output source catalogs and removed any source associated with the radio relic and foreground FR-I source since these sources are larger than the 300 pixel box size for the local noise determination. The source detection was run on all three frequency maps. The locations of the detected sources are indicated on Figure 1.

We then searched for optical counterparts to the radio sources within the area covered by the *HST* CLASH catalog and *HST* Frontier Fields observations. For the detected radio sources, we overlaid the radio contours on an *HST* Frontier Fields color (v1.0[25], F425W, F606W, and F814W band) image to verify that the correct counterparts were identified; see Figures 2 (lensed sources) and 5. Counterparts were found for all radio sources. In a few cases, more than one optical counterpart was identified for the radio source in the CLASH catalog because of the complex morphology of the galaxy in

---
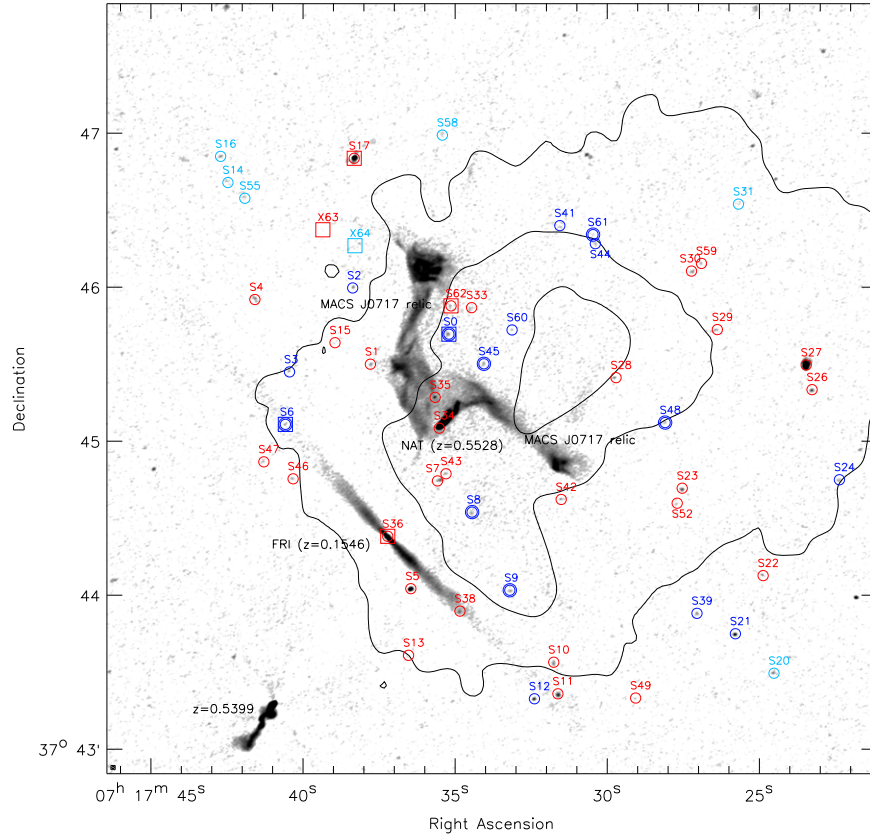
Figure 1. S-band B+A-array image made with robust = 0.75 weighting (Briggs 1995). The image has a resolution of $1''0 \times 0''8$ and a noise level of 1.8 μJy beam^{-1}. Compact radio and X-ray sources that fall within the *HST* coverage are indicated. Blue circles represent objects for which we could confirm that they are located behind the cluster. Blue double circled sources have amplification factors >2 and are individually discussed in Section 3.2. Red circles represent cluster and foreground radio sources. Light blue circled sources have too uncertain redshifts to determine if they are cluster members, foreground objects, or background objects. Boxes indicate X-ray-detected sources, with color coding identical to the radio sources. Black contours show the X-ray emission from *Chandra* smoothed with a Gaussian with a FWHM of $10''$. X-ray contours are drawn at levels of [5, 20, 50]× the background level (determined by measuring the background level around 2.5 Mpc, i.e., $\simeq R_{200}$) from the cluster center. Both sky and instrumental background were included here.

the *HST* images. An overview of all the compact lensed radio sources that were found within the *HST* FOV is given in Table 4. The properties of the sources that are not lensed, or for which we could not determine if they were located behind the cluster, are listed in Table 5.

To detect even fainter radio sources, we combined the individual L-, S-, and C-band images into one deep 1–6.5 GHz wideband continuum image, scaling with a spectral index[26] (α) of -0.5. This was done by convolving all maps to the resolution of the C-band image. With the help of this deep image, we identified about a dozen more sources below the PyBDSM detection threshold in the individual maps, but with peak fluxes above the local $3\sigma_{rms}$. We manually determined the flux densities of these sources in AIPS with the task JMFIT. In addition, we visually identified five more sources in this deep image that were below the $3\sigma_{rms}$ thresholds in the individual maps and thus not recognized there. These sources are also listed in Table 4 (and Table 5). We do not report integrated flux densities for these sources since they are not clearly detected in any of the individual maps. The CLASH photometric redshift and best fitting BPZ (Benítez 2000) spectral template for each source are also listed. For more details on the photometric redshifts and spectral templates, the reader is referred to Molino

et al. (2014) and Jouvel et al. (2014). For 23 sources, spectroscopic redshifts are available from Ebeling et al. (2014).

For the sources that are located at redshifts larger than the cluster, we include the amplification factors in Table 4, taking the average over all the eight publicly available[27] *HST* Frontier Fields lensing models for MACS J0717.5+3745. The amplifications at a given redshift are calculated directly from the mass (κ) and shear (γ) maps. For more details on how these lensing models were derived, we refer to reader to the references provided in Table 4. The reported uncertainties in the amplification factors for the individual models are smaller than the scatter between these models. Therefore, for the uncertainty in the amplification factor, we take the standard deviation between these models, which should better reflect the actual uncertainties.

In total, we find 51 compact radio sources within the area covered by the *HST* imaging. In this sample, 16 sources are located behind the cluster, i.e., those where the 95% confidence limit of the lower redshift bound places it beyond the cluster redshift of $z = 0.5458$. Of these sources, seven have amplification factors larger than 2. We plot the location of the lensed radio and X-ray sources on top of an amplification map for a $z = 2$ source in Figure 3. We used the Zitrin-ltm-Gauss_v1 model amplification map as an example here. We discuss these

---

[26] $F_\nu \propto \nu^\alpha$.

[27] https://archive.stsci.edu/prepds/frontier/lensmodels/
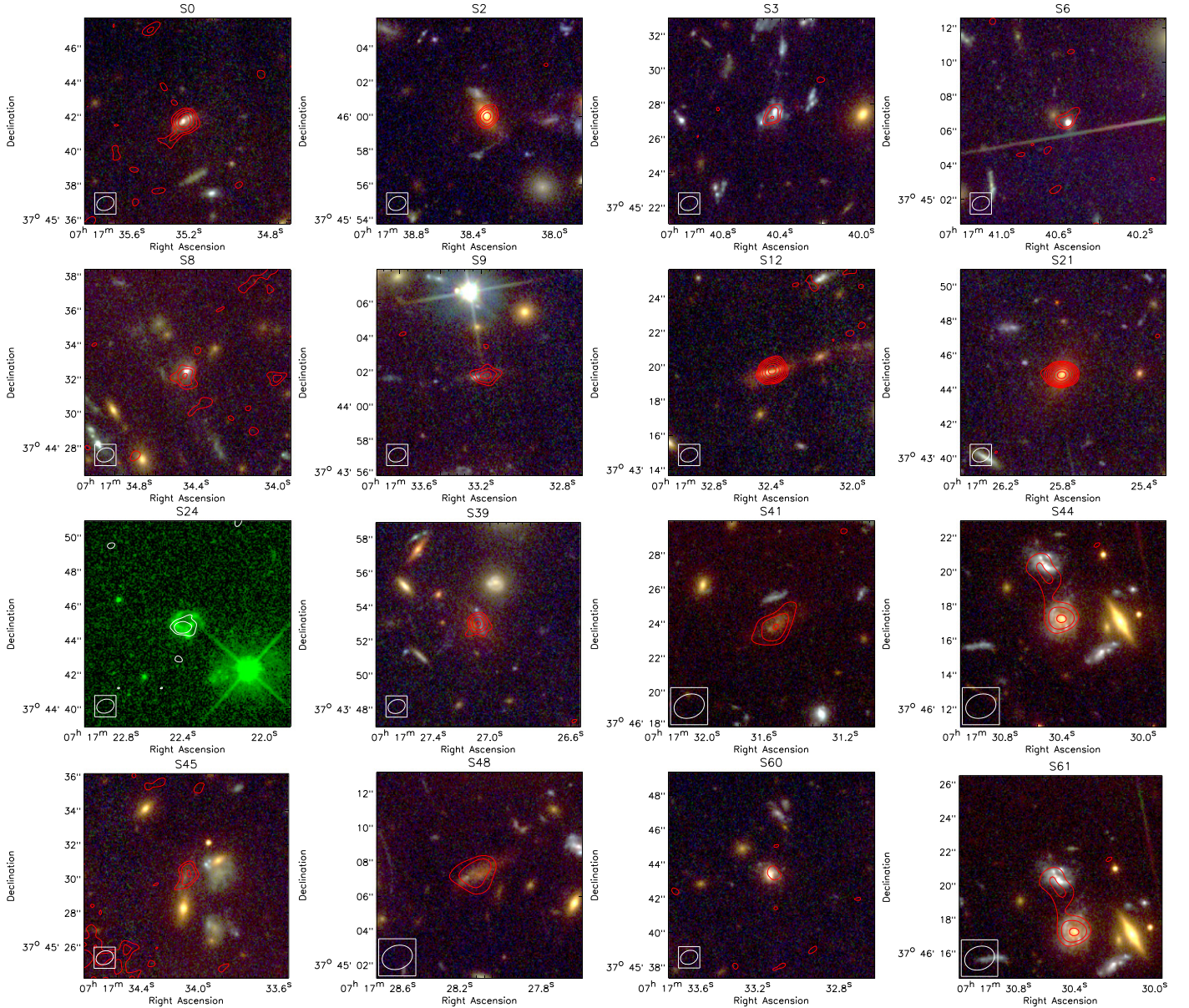
Figure 2. *HST* F435, F606W, and F814W postage stamp color images of the compact lensed radio sources in the MACS J0717.3745 field. Similar postage stamp images, but for sources that are not lensed, are shown in Figure 5. The red radio contours are from the 2–4 GHz S-band image and drawn at levels $\sqrt{([1, 2, 4, \ldots])} \times 3\sigma_{\rm rms}$, with $\sigma_{\rm rms} = 1.8\ \mu{\rm Jy\ beam}^{-1}$. The beam size is indicated in the bottom left corner. We draw white radio contours for some images to aid visibility (in case the area was not covered by all the *HST* filters). For sources without an S-band detection, we overlay contours from the C-band image (if detected there) or the L-band image. We use contours from the combined L-, S-, and C-band images if the source is not detected in any of the three individual band images. The values for $\sigma_{\rm rms}$ for the L- and C-band images are listed in Table 2.

lensed sources with amplification factors larger than 2 in some more detail in Section 3.2. About a dozen radio sources are associated with cluster members (i.e., $0.5 < z_{\rm phot} < 0.6$).

We also search for the presence of compact X-ray sources within the *HST* FOV. In total, we detect seven X-ray sources. Five of these have radio counterparts. The X-ray sources are also included in Table 4, with the measured X-ray fluxes. Two of these X-ray sources which have radio counterparts are lensed by the cluster. The other X-ray sources are foreground objects, cluster members, or have uncertain redshifts.

3.2. Lensed Sources

In this section, we discuss the radio and X-ray properties of the lensed sources with amplification factors >2. These sources

are double circled in Figure 1. For the sources that are not obvious AGNs (i.e., those that do not have X-ray counterparts), we compute the star-formation rate based on the measured radio luminosity. When converting from flux density to luminosity, we used the amplification factors listed in Table 4. The radio luminosity of the galaxies (non-AGN) can be converted to mean star-formation rate over the past $\sim 10^8$ years (Best et al. 2002) using

$$\frac{\rm SFR}{M_\odot\ {\rm yr}^{-1}} \approx 4.5 \left(\frac{\rm GHz}{\nu}\right)^\alpha \frac{L_\nu}{10^{22}\ {\rm W\ Hz}^{-1}}, \quad (1)$$

where L_ν represents the k-corrected rest-frame radio luminosity (which is also corrected for the amplification). The underlying assumptions are that cosmic rays from SNe II trace star-

Table 4
Properties of Cluster Background Sources

Name/ID	R.A. (°) (J2000)	Decl. (°) (J2000)	$S_{1.5}$ (μJy)	$S_{3.0}$ (μJy)	$S_{5.5}$ (μJy)	z_{phot}	t_b	Amplification	X-ray Flux (10^{-15} erg cm^{-2} s^{-1})	z_{spec} Ebeling et al. (2014)
S03358	109.3967560	37.7615846	48.0 ± 11.1	25.9 ± 3.3	11.7 ± 3.9	$1.59^{+0.09}_{-0.06}$	5.90	3.6 ± 1.0	$17.1^{+0.16}_{-0.20}$	1.6852 ± 0.001 (E)
S2 2759	109.4097441	37.7666944	...	21.2 ± 3.2	16.4 ± 3.8	$0.74^{+0.07}_{-0.03}$	5.10	1.25 ± 0.8	...	...
S3 3866	109.4184262	37.7576298	24.4 ± 9.2[a]	19.4 ± 3.1	11.7 ± 3.6	$1.52^{+0.10}_{-0.07}$	9.40	1.8 ± 0.4	...	...
S64614	109.4189706	37.7517924	...	10.1 ± 1.9[b,c]	...	$1.89^{+0.08}_{-0.09}$	6.40	2.3 ± 0.7	$8.48^{+1.24}_{-1.08}$	...
S85637	109.3935136	37.7423563	...	24.0 ± 5.5[a]	...	$1.15^{+0.04}_{-0.03}$	7.70	6.4 ± 1.7	...	...
S96554	109.3882566	37.7338089	43.7 ± 7.9	20.0 ± 3.0	24.9 ± 3.5	$1.69^{+0.22}_{-0.06}$	5.60	3.4 ± 1.0	...	...
S12 7885	109.3850184	37.7221324	96.6 ± 10.5	54.5 ± 3.3	36.9 ± 3.8	$2.32^{+0.14}_{-0.05}$	5.10	1.8 ± 0.5	...	...
S21 7107	109.3575070	37.7291308	86.4 ± 8.8	75.7 ± 3.0	87.1 ± 4.6	$1.02^{+0.15}_{-0.06}$	4.70	1.4 ± 0.3	...	...
S24₁ 5304	109.3430929	37.7459519	...	19.1 ± 3.0	...	$0.9^{+0.3}_{-0.4}$	7.90	1.4 ± 0.2[d,e]	...	...
S24₂ 5307	109.3432347	37.7456667	...	19.1 ± 3.0	...	$0.7^{+0.3}_{-0.3}$	8.80	1.4 ± 0.2[d,e]	...	...
S24₃ 5305	109.3431472	37.7458181	...	19.1 ± 3.0	...	$0.9^{+0.3}_{-0.2}$	8.80	1.4 ± 0.2[d]	...	...
S24₄ 5306	109.3434442	37.7458095	...	19.1 ± 3.0	...	$0.8^{+0.3}_{-0.6}$	6.80	1.4 ± 0.2[d,e]	...	...
S39 6832	109.3626639	37.7313808	26.7 ± 8.6[a]	22.8 ± 3.2	...	$1.1^{+1.5}_{-0.1}$	6.50	1.4 ± 0.2	...	...
S41 1901	109.3813749	37.7733429	...	...	22.6 ± 3.0	$1.02^{+0.07}_{-0.08}$	6.00	1.7 ± 0.3	...	...
S44 2104	109.3766785	37.7714612	...	...	...	$0.82^{+0.06}_{-0.06}$	6.50	1.6 ± 0.3	...	...
S453811	109.3919138	37.7583808	...	22.7 ± 2.6	...	$1.41^{+0.07}_{-0.19}$	6.30	8.7 ± 4.1	...	...
S484567	109.3670705	37.7520604	...	...	...	$0.91^{+0.07}_{-0.06}$	5.40	2.7 ± 0.9	...	...
S60 3367	109.3880803	37.7620638	...	8.3 ± 3.3[a]	...	$0.80^{+0.07}_{-0.05}$	6.80	1.7 ± 0.2	...	...
S61₁2016	109.3770241	37.7723431	...	...	...	$1.73^{+0.09}_{-0.14}$	7.60	3.4 ± 2.5[d]	...	...
S61₂2015	109.3769567	37.7724821	...	...	...	$1.6^{+0.2}_{-0.2}$	8.30	3.4 ± 2.5[d,f]	...	...

Notes. The source ID and positions are taken from the CLASH catalog. The photometric redshifts (z_{phot}) and best fitting spectral template (t_b) are also taken from the CLASH catalog. The photometric redshifts are given at a 95% confidence level. The spectral templates are described in Molino et al. (2014). In total, there are 11 possible spectral templates, 5 for elliptical galaxies (1–5), 2 for spiral galaxies (6, 7), and 4 for starburst galaxies (8–11), along with emission lines and dust extinction. Non-integer values indicate interpolated templates between adjacent templates. For the radio flux density errors, we include a 2.5% uncertainty from bootstrapping the flux density scale. The listed amplification factors are the mean values from the models: CATS_v1 (Jauzac et al. 2012; Richard et al. 2014), Sharon_v2 (Johnson et al. 2014), Zitrin-ltm_v1, Zitrin-ltm-Gauss_v1 (e.g., Zitrin et al. 2013, 2009b), GLAFIC_v3 (Ishigaki et al. 2015), Williams_v1 (e.g., Liesenborgs et al. 2006), Bradac_v1 (Bradač et al. 2005, 2009), Merten_v1 (e.g., Merten et al. 2011). For the spectroscopic redshifts (z_{spec}), the spectral classification is as follows: A—absorption-line spectrum; E—emission-line spectrum.
[a] Manually measured.
[b] Flux density measurement could be affected by radio emission from other sources.
[c] Very faint source, only peak flux was measured.
[d] The complex morphology of the galaxy likely caused it to be fragmented and listed as separate objects in the catalog.
[e] We assume that these source components have the same redshift as S24₃.
[f] We assume that this source component has the same redshift as S61₁.

Table 5
Source Properties

| Name/ID	R.A. (°) (J2000)	Decl. (°) (J2000)	$S_{1.5}$ (μJy)	$S_{3.0}$ (μJy)	$S_{5.5}$ (μJy)	$z_{\rm phot}$	t_b	X-ray Flux (10^{-15} erg cm^{-2} s^{-1})	$z_{\rm spec}$ Ebeling et al. (2014)
S1 3774	109.4073141	37.7583435	47.5 ± 11.2	22.6 ± 3.5	...	$0.46^{+0.07}_{-0.04}$	6.80	...	...
S4 2833	109.4232228	37.7654146	105.7 ± 7.2	60.4 ± 2.2	24.7 ± 3.5	$0.29^{+0.06}_{-0.07}$	5.90	...	...
S5 6341	109.4018584	37.7340578	442.2 ± 9.4	578.1 ± 3.2	446.2 ± 5.1	$0.69^{+0.04}_{-0.10}$	5.50	...	0.5426 ± 0.0003 (E)
S7 5353	109.3982487	37.7457351	157.0 ± 9.2	57.6 ± 3.0	16.3 ± 3.5	$0.54^{+0.11}_{-0.02}$	1.00	...	0.5408 ± 0.0003 (A)
S10 7521	109.3823125	37.7260450	64.4 ± 8.2	40.8 ± 2.5	19.1 ± 3.7	$0.56^{+0.06}_{-0.04}$	6.60	...	0.5315 ± 0.0005 (E)
S11 7828	109.3816839	37.7225923	132.2 ± 9.9	85.3 ± 3.1	51.2 ± 4.3	$0.30^{+0.05}_{-0.07}$	6.00	...	...
S13 7314	109.4023607	37.7268590	...	...	12.7 ± 5.0^a	$0.57^{+0.07}_{-0.04}$	8.20	...	0.5332 ± 0.0003 (E)
S14 1407	109.4268701	37.7779977	43.9 ± 13.5^a	...	...	$0.6^{+3.0}_{-0.4}$	7.90	...	...
S15 3462	109.4122491	37.7606844	35.7 ± 13.4^a	...	...	$0.50^{+0.04}_{-0.04}$	6.80	...	0.4992 ± 0.0003 (E)
S16 1096	109.4278576	37.7808548	66.2 ± 8.7	24.3 ± 3.1	26.9 ± 3.6	$1.0^{+3.1}_{-0.7}$	8.50	...	...
S17 952	109.4095733	37.7806377	1685.9 ± 12.4	1048.8 ± 4.0	847.8 ± 7.9	$0.64^{+0.07}_{-0.05}$	5.50	$5.64^{+0.18}_{-0.15}$	0.5613 ± 0.0003 (A)
S20 7679	109.3522480	37.7248602	38.8 ± 8.7	25.4 ± 3.2	20.1 ± 6.0^a	$0.9^{+3.4}_{-0.5}$	7.90	...	...
S22 6064	109.3537889	37.7355689	26.7 ± 10.2^a	16.5 ± 2.9	...	$0.49^{+0.04}_{-0.05}$	6.00	...	0.5357 ± 0.0003 (E)
S23 5574	109.3647573	37.7448496	90.6 ± 9.3	48.6 ± 3.0	26.8 ± 3.2	$0.55^{+0.03}_{-0.04}$	7.50	...	0.5261 ± 0.0003 (E)
S26 4123	109.3470266	37.7555482	85.0 ± 8.8	50.6 ± 3.2	27.0 ± 3.9	$0.5^{+0.2}_{-0.2}$	6.50	...	0.4212 ± 0.0003 (E)
S27 3789	109.3478763	37.7578892	2013.0 ± 16.1	1274.5 ± 7.8	811.2 ± 9.2	$0.65^{+0.07}_{-0.37}$	7.00	...	...
S28 3852	109.3739700	37.7568547	45.4 ± 10.1	24.6 ± 2.7	15.9 ± 3.5	$0.58^{+0.03}_{-0.03}$	5.60	...	0.5565 ± 0.0003 (E)
S29 3402	109.3598798	37.7621055	...	19.7 ± 4.6^a	17.0 ± 5.7^a	$0.55^{+0.04}_{-0.03}$	5.40	...	0.5442 ± 0.0003 (A)
S30 2446	109.3634032	37.7683109	33.5 ± 12.5^a	31.5 ± 4.6	19.6 ± 3.2	$0.15^{+0.03}_{-0.05}$	6.80	...	...
S31 1660	109.3568926	37.7756024	...	...	14.4 ± 5.8^a	$0.9^{+2.9}_{-0.7}$	7.90	...	...
S33 2974	109.3936629	37.7644686	...	...	...	$0.34^{+0.06}_{-0.03}$	6.80	...	...
S34 4426	109.3981162	37.7514879	17797 ± 29	7058 ± 14	3149 ± 9	$0.56^{+0.03}_{-0.02}$	5.50	...	0.5528 ± 0.0003 (A)
S35 4020	109.3985608	37.7547888	$59.79 \pm 5.1^{a,b}$	41.8 ± 8.0^b	$25.2 \pm 2.4^{a,b}$	$0.54^{+0.04}_{-0.02}$	4.30	...	0.5443 ± 0.0003 (A)
S36 5598	109.4050484	37.7397125	10505 ± 71	8356 ± 36	7132 ± 24	$0.16^{+0.06}_{-0.02}$	1.30	$5.88^{+0.15}_{-0.14}$	...
S38 6779	109.3951581	37.7315723	$38.4 \pm 4.9^{a,b,c}$	29.1 ± 6.7	$29.5 \pm 2.4^{a,b,c}$	$0.53^{+0.03}_{-0.05}$	4.40	...	0.5366 ± 0.001 (A)
S42 5335	109.3813319	37.7437654	31.6 ± 11.2^a	13.2 ± 3.1	...	$0.48^{+0.03}_{-0.03}$	5.50	...	0.4919 ± 0.0003 (E)
S43 4992	109.3970833	37.7464913	...	19.8 ± 3.1	8.5 ± 3.3	$0.54^{+0.04}_{-0.03}$	6.20	...	0.1779 ± 0.0003 (E)
S46 5274	109.4179222	37.7459331	36.3 ± 13.2^a	23.0 ± 2.6	...	$0.50^{+0.04}_{-0.04}$	9.40	...	0.5490 ± 0.0003 (E)
S47 5076	109.4220234	37.7478226	33.0 ± 12.3^a	21.1 ± 6.8	...	$0.54^{+0.06}_{-0.05}$	6.30	...	0.5660 ± 0.0003 (E)
S49 7693	109.3710599	37.7222104	...	$7.5 \pm 1.9^{a,c}$	...	$0.30^{+0.09}_{-0.18}$	6.40	...	0.2288 ± 0.0003 (E)
S52 5299	109.3654725	37.7433269	105.0 ± 6.2	...	...	$0.22^{+0.03}_{-0.03}$	7.00	...	...
S55$_1$ 1585^d	109.4246322	37.7763075	...	...	...	$0.4^{+2.5}_{-0.3}$	8.00	...	...
S55$_2$ 1584^d	109.4245383	37.7763555	...	...	...	$2.5^{+0.6}_{-2.2}$	7.90	...	...
S58 792	109.3976281	37.7831987	...	...	12.1 ± 5.2^a	$0.8^{+1.1}_{-0.4}$	7.60	...	...
S59 2444	109.3621323	37.7692569	...	13.5 ± 4.3^a	...	$0.56^{+0.08}_{-0.05}$	6.50	...	0.4984 ± 0.0005 (A)
S62 2977	109.3963967	37.7646847	...	19.9 ± 5.4^a	...	$0.65^{+0.03}_{-0.05}$	6.80	$3.09^{+0.98}_{-0.84}$	0.5490 ± 0.0005 (E)
X63 1956	109.4139432	37.7728903	...	...	...	$0.50^{+0.06}_{-0.03}$	5.20	$7.37^{+3.87}_{-2.87}$	0.4897 ± 0.0003 (A)
X64$_1$ 2220^d	109.4099881	37.7711734	...	...	...	$0.8^{+3.1}_{-0.5}$	8.00	$6.20^{+3.09}_{-4.71}$	...
X64$_2$ 2222^d	109.4095458	37.7711695	...	...	...	$0.6^{+3.1}_{-0.2}$	8.70	$6.20^{+3.09}_{-4.71}$	...

Notes. The source ID and positions are taken from the CLASH catalog. The photometric redshifts ($z_{\rm phot}$) and best fitting spectral template (t_b) are also taken from the CLASH catalog. The photometric redshifts are given at a 95% confidence level. The spectral templates are described in Molino et al. (2014). In total, there are 11 possible spectral templates, 5 for elliptical galaxies (1–5), 2 for spiral galaxies (6, 7), and 4 for starburst galaxies (8–11), along with emission lines and dust extinction. Non-integer values indicate interpolated templates between adjacent templates. For the radio flux density errors, we include a 2.5% uncertainty from bootstrapping the flux density scale. For the spectroscopic redshifts ($z_{\rm spec}$), the spectral classification is as follows: A—absorption-line spectrum; E—emission-line spectrum.
^{a} Manually measured.
^{b} Flux density measurement could be affected by radio emission from other sources.
^{c} Very faint source, only peak flux was measured.
^{d} The complex morphology of the galaxy likely caused it to be fragmented and listed as separate objects in the catalog.
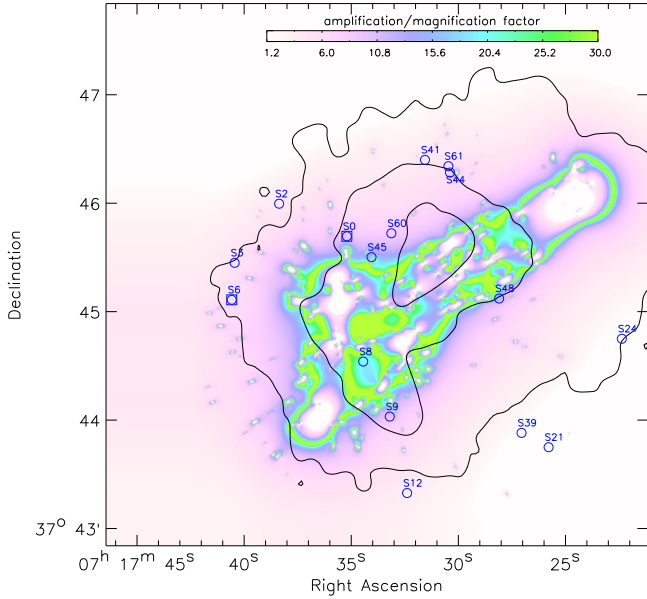
Figure 3. Amplification/magnification map for a $z = 2$ source from the `Zitrin-ltm-Gauss_v1` lensing model. For details of the lens modeling, see Zitrin et al. (2009b). The location of the background compact sources are indicated as in Figure 1. Black contours show the X-ray emission from *Chandra*, smoothed with a Gaussian with a FWHM of 10″. X-ray contours are drawn at levels of $[5, 20, 50]\times$ the X-ray background level as in Figure 1.

forming regions and that the number of SNe II is directly proportional to the SFR. An advantage of these radio-derived SFRs is that they are not significantly affected by dust extinction. For our sources, we use the 3 GHz measurement (unless stated otherwise), scaling with a spectral index of $\alpha = -0.5$. The uncertainty in the radio-derived SFR is about a factor of 2 (Bell 2003).

We can also compute the specific SFRs (sSFR) by computing the stellar mass ($M_\star$) from the *Spitzer* 3.6 and 4.5 μm fluxes, following the approach by Rawle et al. (2014). We corrected these fluxes for the amplification and computed the K-correction using the BPZ spectral templates. The *Spitzer* fluxes are taken from SEIP Source List (Enhanced Imaging Products from the *Spitzer* Heritage Archive; we took the 3″.8 diameter aperture flux densities). To compute the stellar mass, we use the relation from Eskew et al. (2012)

$$M_*[M_\odot] = 10^{5.65} S_{3.6\,\mu m}^{2.85} S_{4.5\,\mu m}^{-1.85} (D_L/0.05)^2 , \qquad (2)$$

where S_λ is in units of Jy, and D_L the luminosity distance in megaparsecs. This relation was derived for the Large Magellanic Cloud and assumes a Salpeter (1955) initial mass function (IMF). It may break down for more strongly star-forming systems and might also vary with metallicity. Therefore, Equation (2) should be taken as an approximation to the stellar mass.

3.2.1. Comments on Individual Sources

The source S0 has a spectroscopically measured redshift of 1.6852 ± 0.001 (Ebeling et al. 2014) and an amplification factor of 3.6 ± 1.0 The source is associated with a disk galaxy that has a central bright core in the *HST* image. The source is also detected with *Chandra* (171 ± 25 net counts) with an unabsorbed 2–10 keV flux of $1.71^{+0.16}_{-0.20} \times 10^{-14}$ erg s^{-1} cm^{-2}.

The photon index of the power law of was determined at $0.89^{+0.33}_{-0.42}$. Together with the amplification factor and associated uncertainty, this translates into a rest-frame luminosity of $0.29^{+0.11}_{-0.07} \times 10^{44}$ erg s^{-1}, typical of an AGN. The optical spectrum of the galaxy contains emission lines and the best fitting BPZ template is that of an Sbc-type spiral galaxy.

Source S6 seems to be associated with a compact star-like object. We also find an X-ray counterpart to the source (150 ± 12 net counts). The object has a $z_{\rm phot} = 1.89^{+0.08}_{-0.09}$ and an amplification factor of 2.3 ± 0.7. With this amplification factor and redshift, the unabsorbed 2–10 keV flux of $8.48^{+1.24}_{-1.08} \times 10^{-15}$ erg s^{-1} cm^{-2} translates to a rest-frame luminosity of $0.88^{+0.41}_{-0.25} \times 10^{44}$ erg s^{-1}. The photon index of the power law of was determined at $2.05^{+0.24}_{-0.23}$. The best fitting BPZ template was that of a spiral galaxy, but the χ^2 value of 29.3 indicated a very poor fit. Given the star-like nature of the object and poor fit, this source could be a quasar.[28]

S8 is located at $z_{\rm phot} = 1.15^{+0.04}_{-0.03}$ and has a high amplification factor of about 6.4 ± 1.8. The best fitting BPZ template is that of a starburst galaxy. Based on the S-band radio flux, we compute a SFR of 15^{+12}_{-7} $M_\odot$ yr^{-1}. With $M_* = 2.4^{+1.4}_{-1.0} \times 10^{10}$ $M_\odot$ we compute a sSFR of $0.6^{+0.4}_{-0.3}$ Gyr^{-1}. The errors take into account the uncertainties in the radio and *Spitzer* flux density measurements, amplification factor (Table 4), and redshift. For the radio spectral index, we assumed an uncertainty of $\Delta\alpha = 0.3$. Errors where estimated via a Monte Carlo approach, drawing 10^4 realizations. Note that M_*, SFR, and sSFR are computed under the assumption that Equations (1) and (2) hold.

S9 is associated with a faint red galaxy with $z_{\rm phot} = 1.69^{+0.22}_{-0.06}$ and is amplified with a factor of 3.4 ± 1.0. The best fitting BPZ template corresponds to a Sbc/ES0 galaxy. The source has a relatively flat spectral index of $\alpha = -0.4 \pm 0.2$ between 1.5 and 5.5 GHz. Based on the integrated flux density, we compute a high SFR of 49^{+46}_{-21} $M_\odot$ yr^{-1}, scaling with $\alpha = -0.4$. A blue galaxy is located about $1''$ to the east of this galaxy at $z_{\rm photo} = 1.70^{+0.12}_{-0.14}$. With $M_* = 4.5^{+3.3}_{-1.9} \times 10^{10}$ $M_\odot$ we compute a sSFR of $1.1^{+0.8}_{-0.5}$ Gyr^{-1}.

S45 is associated with a faint red galaxy with $z_{\rm phot} = 1.41^{+0.06}_{-0.19}$. It has a high amplification factor of 8.7 ± 4.1 with a best fitting spiral galaxy spectral template. We compute a SFR of 17^{+29}_{-11} $M_\odot$ yr^{-1}.

In addition to the above sources that were detected in the individual L-, S-, or C-band images, we also found two sources in the deep broad-band stacked radio image with amplifications >2. S48 is associated with a red galaxy at $z_{\rm photo} = 0.91^{+0.07}_{-0.06}$, with an amplification factor that is slightly less than 3. It is best fit by a spiral BPZ template. S61 is associated with a blue irregular galaxy. Its amplification factor is 3.4 ± 2.5 and the best fitting spectral template is that of a starburst galaxy. It is listed as two separate objects in the CLASH photometric catalog, with component 2 (Table 4) being a bright "knot" to the north, embedded within the overall emission from the galaxy (component 1). Thus, the *HST* images suggest that both components belong the same galaxy with a complex morphology. This is also consistent with the two photometric redshifts that indicate $z_{\rm photo} \approx 1.6$.

It should be acknowledged that some of the sources we identify here, particularly those that lay behind the cluster according to their photometric redshifts, may be multiple

---

[28] Note that the BPZ fitting did not include AGNs or quasar galaxy templates.

images of multiply lensed background sources. A brief search according to the predictions of the model seen in Figure 3 neither assigned sources listed here to the same multiply imaged sources, nor were other counter images located. We also cross-checked the position of our lensed sources against the list of multiply lensed sources by Limousin et al. (2012), but none of our sources appear in this list. This means that—adopting the lens model in hand—either the photometric redshift for these images significantly deviate than those listed in Table 4, or that the predicted counter images's flux is below the detection limit given a possibly smaller magnification, for example. A more dedicated examination and search for multiple images among our sample will be performed elsewhere.

3.3. Radio Luminosity Function

It is expected that the number of star-forming galaxies increases with redshift, peaking at $z \sim 2$ (e.g., Madau & Dickinson 2014). We compute the radio luminosity function from the sources detected in our S-band image that have a 3 GHz flux density above 18 μJy ($10 \times \sigma_{\rm rms}$). Above this flux density, we should be reasonably complete also for sources that are resolved.

For the luminosity function, we determine the volume behind the cluster in which we could detect a hypothetical source above the flux limit for a given luminosity. We then divide the number of detected sources (for that luminosity range) by the obtained volume. To compute the volume, we take the varying magnification (as a function of position and redshift) into account using the publicly available lensing models and provided `Python` code.

We excluded the regions covered by the radio relic. We scaled our 3 GHz S-band luminosities to 1.4 GHz taking $\alpha = -0.5$, to facilitate a comparison with the literature results from Best et al. (2005). We limited ourselves to the range $0.6 < z < 2.0$, because we only detect a single source above $z > 2$. Restricting the redshift range also limits the effects of the redshift evolution of the radio luminosity function.

The differences between the lensing models are larger than the uncertainties provided for the individual models. We therefore compute the volume for each for the eight models listed in Table 4 and take the average. The same is done for counting the number of sources in each luminosity bin (as this also depends on the amplification factors). In Figure 4 we plot the luminosity function averaged over these eight different lensing models. The red error bars represent the standard deviation over the eight lensing models. The black error bars show the combined uncertainty from the lensing models and Poisson errors on the galaxy number counts. These two errors were added in quadrature. We find that the uncertainties in the redshifts and flux density measurements do not contribute significantly to the error budget.

Another uncertainty for the derived luminosity function is related to cosmic variance. Based on the computed volume, we probe for the three luminosity bins and the number of objects in each bin, we compute the cosmic variance using Trenti & Stiavelli (2008). From this computation, we find that cosmic variance introduces an extra uncertainty between 22% and 30%. Note, however, that this is a factor of a few smaller the Poisson errors and scatter due to the different lensing models.

In Figure 4 we also plot the low-redshift ($z < 0.3$) luminosity function derived by Best et al. (2005). Although
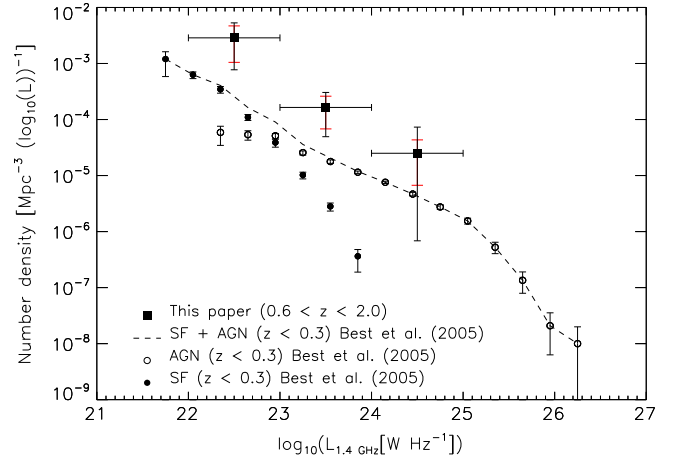

Figure 4. Radio luminosity function (number density of sources) at $0.6 < z < 2.0$ derived from our detected S-band sources. The luminosities were scaled to 1.4 GHz and averaged over all eight lensing models. The uncertainties in black are shown at 1σ and include the Poisson errors and scatter between the eight different lensing models. For reference, the red error bars only show the scatter (standard deviation) in the luminosity function from the eight different lensing models. Results from Best et al. (2005) for a $z < 0.3$ sample are also shown. The Best et al. sample is divided into SF galaxies and AGNs.

the uncertainties in our luminosity function are substantial, we find evidence for an increase in the number density of sources of a factor between 4 and 10 compared to the Best et al. low-redshift sample.

With a larger sample (for example, including all six Frontier Fields clusters), it should become possible to map out the luminosity function more accurately, as the Poisson errors can be reduced by a factor of $\sim\sqrt{6}$. Surveys covering a larger area will be needed to map out the high-luminosity end. These surveys can be shallower and do not require the extra amplification by lensing. A major limitation of the precision that can be achieved for the faint end of the luminosity function, which can only be accessed with the power of lensing, is the accuracy of the lensing models. This highlights the importance of further improving the precision of the Frontier Fields lensing models (see also Limousin et al. 2015).

4. DISCUSSION AND CONCLUSIONS

In our *JVLA* radio images of MACS J0717.5+3745, we discovered seven lensed sources with expected amplification factors larger than 2. This makes MACS J0717.5+3745 the cluster with the largest number of known lensed radio sources. Two of these radio sources are also detected in our *Chandra* X-ray image. To our knowledge, only two other lensed X-ray sources behind a galaxy cluster are known (Abell 370; Bautz et al. 2000). All of the lensed sources (with amplification factors >2) are located at $1 \lesssim z \lesssim 2$ and most seem to be star-forming galaxies with SFR of $\sim$10–50 $M_\odot$ yr^{-1} based on their radio continuum fluxes. Our search for lensed radio sources is different from previous radio studies performed by, e.g., Smail et al. (1997), Garrett et al. (2005), Ivison et al. (2010a, 2010b), and Berciano Alba et al. (2010), which targeted previously known lensed submillimeter galaxies that have SFR $\sim 10^2$–10^3 $M_\odot$ yr^{-1}. The two lensed sources that are also detected in
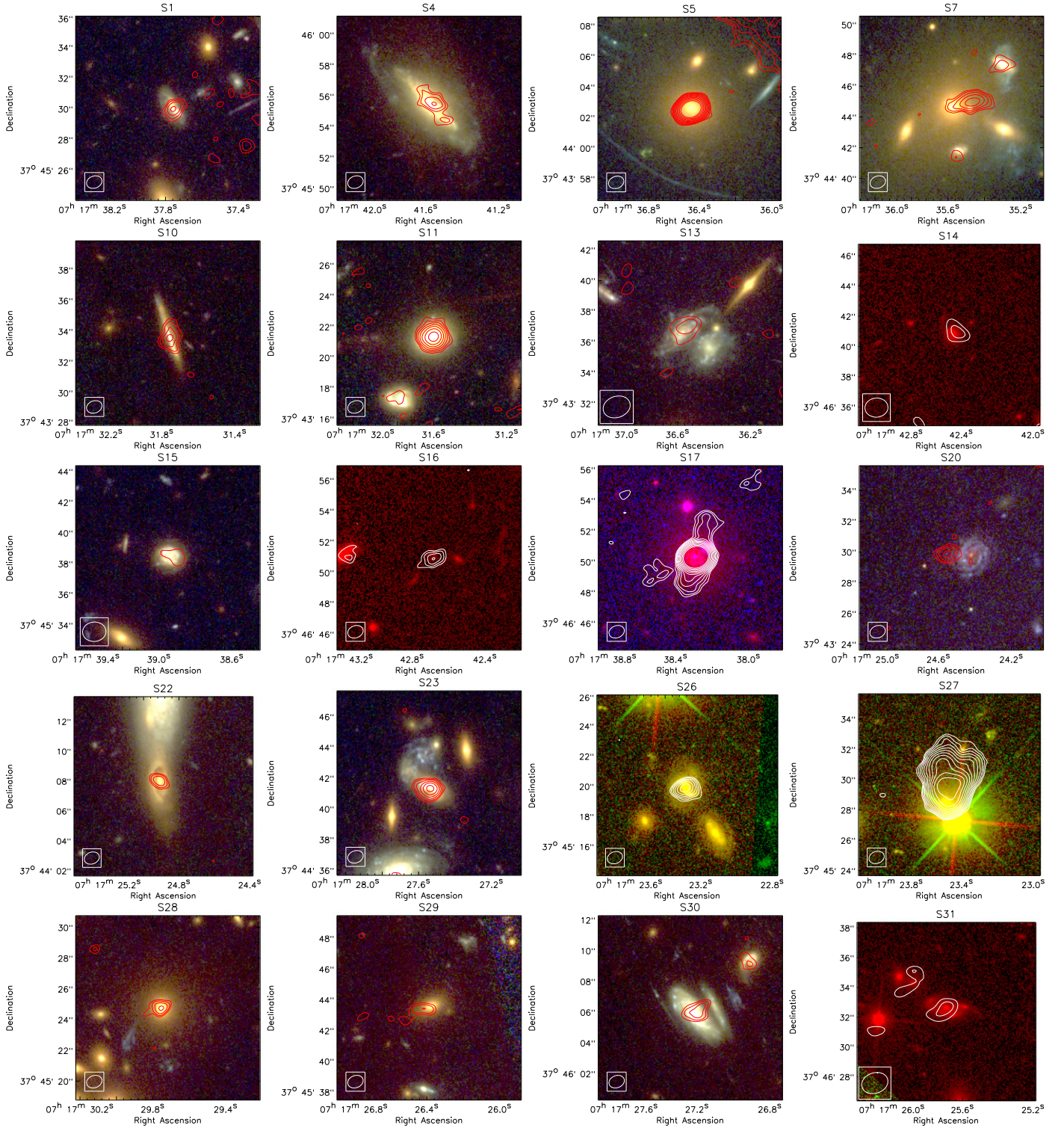
Figure 5. *HST* F435, F606W, and F814W postage stamp color images around the compact radio sources in the MACS J0717.3745 field. The sources in this panel are cluster members, foreground objects, or sources with uncertain redshifts (so that we could not determine whether or not they are lensed). Postage stamp images for the lensed sources are shown in Figure 2. The red radio contours are from the 2–4 GHz S-band image and drawn at levels $\sqrt{([1, 2, 4, \ldots])} \times 3\sigma_{rms}$, with $\sigma_{rms} = 1.8~\mu$Jy beam^{-1}. The beam size is indicated in the bottom left corner. We draw white radio contours for some images to aid visibility (in case the area was not covered by all the *HST* filters). For sources without an S-band detection, we overlay contours from the C-band image (if detected there) or L-band image. We use contours from the combined L-, S-, and C-band images if the source is not detected in any of the three individual band images. The values for σ_{rms} for the L- and C-band images are listed in Table 2. Note that for source S20 there is a very faint CLASH counterpart located precisely at the radio position.

our *Chandra* image have 2–10 keV X-ray luminosities of $\sim 10^{43-44}$ erg s^{-1}. We therefore classify these sources as AGNs (e.g., Bauer et al. 2004).

From the derived luminosity function, we find evidence for an increase in the number density of $0.6 < z < 2.0$ radio sources compared to the $z < 0.3$ sample from Best et al.
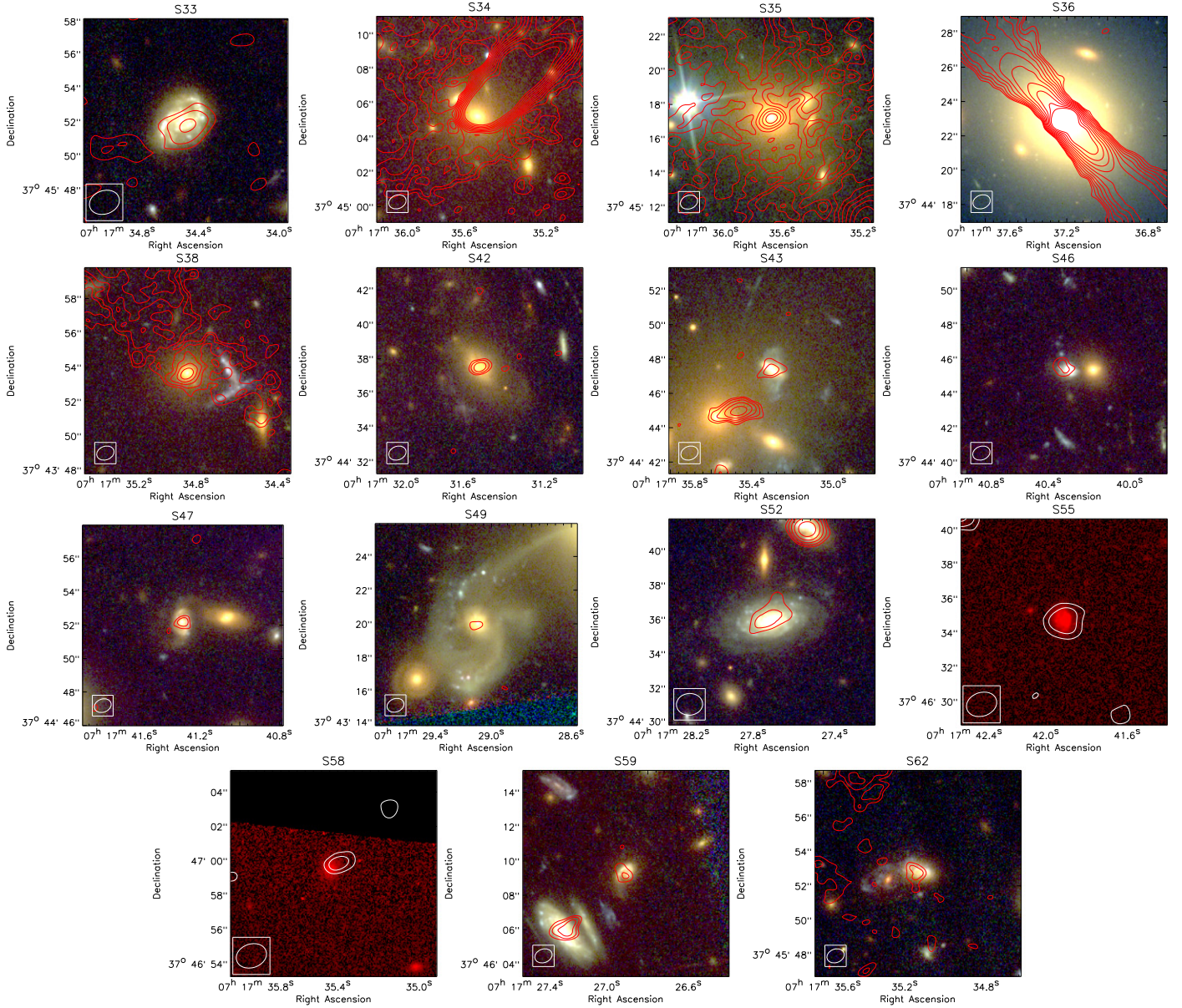
Figure 5. (Continued.)

(2005). The increase is expected given the cosmic evolution of AGNs and SF galaxies between these two redshift ranges (e.g., Best et al. 2014; Madau & Dickinson 2014). Besides the Poisson errors, we find that the scatter between the available lensing models contributes significantly to the uncertainty in our derived luminosity function.

From our *JVLA* observations, we conclude that, as expected, lensing by massive (merging) clusters enables studying star-forming galaxies at moderate to high redshifts, with the advantage of not being affected by extinction. Some of these radio sources have flux densities that are below the detection limits of typical radio observations without the amplification by lensing. In the case of MACS J0717.5+3745, our highest amplification factor is about 9. To detect a source with a similar signal-to-noise ratio in the S-band, without the lensing amplification, would have required about $10 \times 8^2 \approx 600$ hr of *JVLA* integration time. Practically, this means that the Square Kilometre Array (SKA) would be the only instrument

that could achieve such a detection without the help of lensing. This example is similar to the lensed radio source found by Jackson (2011). Radio observations also nicely complement far-infrared and submillimeter observations that can detect strongly star-forming galaxies behind clusters (e.g., Egami et al. 2010; Rawle et al. 2015).

Besides the amplification of the integrated flux density, the lensing magnification offers a chance to study these lensed sources at high spatial resolution. In the case of MACS J0717.5 +3745, all lensed radio sources are not or only slightly resolved at the current ~1″ resolution. A larger sample of lensing clusters is needed to increase the chances of finding a rare bright and more highly magnified source that would allow a detailed spatially resolved study. Based on our MACS J0717.5+3745 result, for a massive lensing cluster (for example, from the CLASH sample), we expect to detect about a handful of lensed radio sources with a pointed ~10 hr *JVLA* observation.

Detection of background lensed X-ray sources suffer from the increased X-ray background from the cluster's ICM, in particular in regions of high magnification (see Figure 3). This makes X-ray observations of lensed sources comparatively less efficient than optical or radio observations. In principle, by choosing a harder energy band (i.e., 2–10 keV), the contrast between a typical AGN and the ICM emission can be increased. However, for massive lensing clusters, this does not work so well because they are generally quite hot ($\sim$5–10 keV), producing significant ICM emission in the hard X-ray band. In addition, the number density of X-ray sources on the sky that could potentially be lensed by a cluster and detected with current instruments with reasonable exposure times is typically lower than that of radio observations and thus decreases the chance of finding an object at high magnification (e.g., Brunner et al. 2008; Condon et al. 2012). Extrapolating from our MACS J0717.5+3745 result, we expect to find of the order of one lensed X-ray object (amplification $\gtrsim 2$) per massive lensing cluster for a $\sim 10^2$ ks *Chandra* observation.

APPENDIX
COMPACT SOURCES:
CLUSTER AND FOREGROUND OBJECTS

In Table 5 we list the properties of all the radio and X-ray sources that are cluster members, foreground objects, or sources with uncertain redshifts (so that we could not determine whether or not they are lensed). We also provide *HST* color postage stamp images around these radio sources in Figure 5.

REFERENCES

Bauer, F. E., Alexander, D. M., Brandt, W. N., et al. 2004, AJ, 128, 2048
Bautz, M. W., Malm, M. R., Baganoff, F. K., et al. 2000, ApJL, 543, L119
Bell, E. F. 2003, ApJ, 586, 794
Benítez, N. 2000, ApJ, 536, 571
Berciano Alba, A., Koopmans, L. V. E., Garrett, M. A., Wucknitz, O., & Limousin, M. 2010, A&A, 509, A54
Best, P. N., Kauffmann, G., Heckman, T. M., & Ivezić, Ž 2005, MNRAS, 362, 9
Best, P. N., Ker, L. M., Simpson, C., Rigby, E. E., & Sabater, J. 2014, MNRAS, 445, 955
Best, P. N., van Dokkum, P. G., Franx, M., & Röttgering, H. J. A. 2002, MNRAS, 330, 17
Bonafede, A., Feretti, L., Giovannini, G., et al. 2009, A&A, 503, 707
Bradač, M., Schneider, P., Lombardi, M., & Erben, T. 2005, A&A, 437, 39
Bradač, M., Treu, T., Applegate, D., et al. 2009, ApJ, 706, 1201
Briggs, D. S. 1995, PhD thesis, New Mexico Institute of Mining Technology Socorro
Brunner, H., Cappelluti, N., Hasinger, G., et al. 2008, A&A, 479, 283
Cash, W. 1979, ApJ, 228, 939
Condon, J. J. 1992, ARA&A, 30, 575
Condon, J. J., Cotton, W. D., Fomalont, E. B., et al. 2012, ApJ, 758, 23
Cornwell, T. J., Golap, K., & Bhatnagar, S. 2005, in ASP Conf. Ser. 347, Astronomical Data Analysis Software and Systems XIV, ed. P. Shopbell, M. Britton, & R. Ebert (San Francisco, CA: ASP), 86
Cornwell, T. J., Golap, K., & Bhatnagar, S. 2008, ISTSP, 2, 647
Ebeling, H., Barrett, E., & Donovan, D. 2004, ApJL, 609, L49
Ebeling, H., Barrett, E., Donovan, D., et al. 2007, ApJL, 661, L33
Ebeling, H., Edge, A. C., & Henry, J. P. 2001, ApJ, 553, 668
Ebeling, H., Ma, C.-J., & Barrett, E. 2014, ApJS, 211, 21
Edge, A. C., Ebeling, H., Bremer, M., et al. 2003, MNRAS, 339, 913
Egami, E., Rex, M., Rawle, T. D., et al. 2010, A&A, 518, L12
Eskew, M., Zaritsky, D., & Meidt, S. 2012, AJ, 143, 139
Fanaroff, B. L., & Riley, J. M. 1974, MNRAS, 167, 31P
Garn, T., Green, D. A., Riley, J. M., & Alexander, P. 2009, MNRAS, 397, 1101
Garrett, M. A., Knudsen, K. K., & van der Werf, P. P. 2005, A&A, 431, L21
Ishigaki, M., Kawamata, R., Ouchi, M., et al. 2015, ApJ, 799, 12
Ivison, R. J., Smail, I., Papadopoulos, P. P., et al. 2010a, MNRAS, 404, 198
Ivison, R. J., Swinbank, A. M., Swinyard, B., et al. 2010b, A&A, 518, L35
Jackson, N. 2011, ApJL, 739, L28
Jauzac, M., Jullo, E., Kneib, J.-P., et al. 2012, MNRAS, 426, 3369
Johnson, T. L., Sharon, K., Bayliss, M. B., et al. 2014, ApJ, 797, 48
Jouvel, S., Host, O., Lahav, O., et al. 2014, A&A, 562, A86
Kalberla, P. M. W., Burton, W. B., Hartmann, D., et al. 2005, A&A, 440, 775
Kneib, J.-P., & Natarajan, P. 2011, A&ARv, 19, 47
Liesenborgs, J., De Rijcke, S., & Dejonghe, H. 2006, MNRAS, 367, 1209
Limousin, M., Ebeling, H., Richard, J., et al. 2012, A&A, 544, A71

Limousin, M., Richard, J., Jullo, E., et al. 2015, arXiv:1510.08077
Ma, C., Ebeling, H., & Barrett, E. 2009, ApJL, 693, L56
Ma, C.-J., Ebeling, H., Donovan, D., & Barrett, E. 2008, ApJ, 684, 160
Madau, P., & Dickinson, M. 2014, ARA&A, 52, 415
McMullin, J. P., Waters, B., Schiebel, D., Young, W., & Golap, K. 2007, in
    ASP Conf. Ser. 376, Astronomical Data Analysis Software and Systems
    XVI, ed. R. A. Shaw, F. Hill, & D. J. Bell (San Francisco, CA: ASP), 127
Medezinski, E., Umetsu, K., Nonino, M., et al. 2013, ApJ, 777, 43
Merten, J., Coe, D., Dupke, R., et al. 2011, MNRAS, 417, 333
Mohan, N., & Rafferty, D. 2015, ascl soft, 02007
Molino, A., Benítez, N., Moles, M., et al. 2014, MNRAS, 441, 2891
Offringa, A. R., de Bruyn, A. G., Biehl, M., et al. 2010, MNRAS, 405, 155
Ogrean, G. A., van Weeren, R. J., Jones, C., et al. 2015, ApJ, 812, 153
Perley, R. A., & Butler, B. J. 2013, ApJS, 204, 19
Postman, M., Coe, D., Benítez, N., et al. 2012, ApJS, 199, 25

Rau, U., & Cornwell, T. J. 2011, A&A, 532, A71
Rawle, T. D., Altieri, B., Egami, E., et al. 2014, MNRAS, 442, 196
Rawle, T. D., Altieri, B., Egami, E., et al. 2015, arXiv:1508.00586
Richard, J., Jauzac, M., Limousin, M., et al. 2014, MNRAS, 444, 268
Salpeter, E. E. 1955, ApJ, 121, 161
Smail, I., Ivison, R. J., & Blain, A. W. 1997, ApJL, 490, L5
Trenti, M., & Stiavelli, M. 2008, ApJ, 676, 767
Umetsu, K., Medezinski, E., Nonino, M., et al. 2014, ApJ, 795, 163
Wachter, K., Leach, R., & Kellogg, E. 1979, ApJ, 230, 274
Willingale, R., Starling, R. L. C., Beardmore, A. P., Tanvir, N. R., &
    O'Brien, P. T. 2013, MNRAS, 431, 394
Zitrin, A., Broadhurst, T., Rephaeli, Y., & Sadeh, S. 2009a, ApJL,
    707, L102
Zitrin, A., Broadhurst, T., Umetsu, K., et al. 2009b, MNRAS, 396, 1985
Zitrin, A., Meneghetti, M., Umetsu, K., et al. 2013, ApJL, 762, L30